Pd:In-Doped TiO2 as a Bifunctional Catalyst for the Photoelectrochemical Oxidation of Paracetamol and Simultaneous Green Hydrogen Production

NICOLÁS SACCO , ALEXANDER IGUINI , Ilaria Gamba , Fernanda Albana Marchesini , GONZALO GARCÍA *

Posted Date: 31 January 2024

doi: 10.20944/preprints202401.2169.v1

Keywords: PdIn-doped TiO2 catalyst; green H2 production; photoelectrochemical oxidation; paracetamol; pharmaceutical removal from water.

Article

Pd:In-Doped TiO_2 as a Bifunctional Catalyst for the Photoelectrochemical Oxidation of Paracetamol and Simultaneous Green Hydrogen Production

Nicolás Alejandro Sacco [1,*], Alexander Iguini [2], Ilaria Gamba [2], Fernanda Albana Marchesini [1] and Gonzalo García [2,*]

[1] Instituto de Investigaciones en Catálisis y Petroquímica, INCAPE (UNL-CONICET), Facultad de Ingeniería Química, Santiago del Estero 2829, 3000 Santa Fe, Argentina.
[2] Instituto Universitario de Materiales y Nanotecnología, Departamento de Química, Universidad de La Laguna (ULL), PO Box 456, 38200, La Laguna, Santa Cruz de Tenerife, España.
* Correspondence: ggarcia@ull.edu.es; nsacco@fiq.unl.edu.ar

Abstract: The integration of clean energy generation with wastewater treatment holds promise for addressing both environmental and energy concerns. Focusing on photocatalytic hydrogen production and wastewater treatment, the study introduces PdIn/TiO_2 catalysts for the simultaneous removal of the pharmaceutical contaminant paracetamol and hydrogen production. Physicochemical characterization showed a high distribution of Pd and In on the support as well as a high interaction with it. The Pd and In deposition enhances the light absorption capability and significantly improved HER in comparison to TiO_2 not only in the electrolyte but also in presence of paracetamol. Regarding PTM oxidation, TiO_2 and PdIn/TiO_2 showed an irreversible behavior toward the PTM oxidation, limited by the adsorption of species on the electrode surface. Thus, PdIn-doped TiO_2 stands out as a promising catalyst, showcasing enhanced physicochemical properties and superior catalytic performance. This underscores its potential for both environmental remediation and sustainable hydrogen production.

Keywords: PdIn-doped TiO_2 catalyst; green H_2 production; photoelectrochemical oxidation; paracetamol; pharmaceutical removal from water

1. Introduction

Energy production and water availability pose significant challenges for future generations. The global consumption of both resources is experiencing substantial growth, driven by population increases and improved living standards. The combustion of fossil fuels releases greenhouse gases and other pollutants into the atmosphere, resulting in critical consequences for the environment. On the other hand, water availability is threatened by the presence of contaminants in wastewater and the lack of water sanitation solutions.

The Sustainable Development Goals (SDGs) set forth by the United Nations for 2030 include specific objectives related to energy consumption (SDG 7: Affordable and Clean Energy) and water pollution (SDG 6: Clean Water Sanitation). Renewable energies could be a key part of the solution for sustainable energy production, provided that electricity storage is ensured. Hydrogen has emerged as a highly promising renewable fuel due to its high energy content, lack of environmental hazards, and, most importantly, its ability to be produced from water [1,2]. The production of green hydrogen is a promising way to supply and distribute intermittently generated energy through fuel cells. However, its production through water splitting is not cost-effective due to the large amounts of energy required for the oxygen evolution reaction at the anode. Photo electrocatalytic production of hydrogen by oxidizing organic or inorganic compounds at the anode can be achieved without the need for electrical input, but current catalysts do not meet the requirements to approach viability

 doi:10.20944/preprints202401.2169.v1

goals. It is important to take into account that in the case of water splitting, the potential needed to break down water into oxygen and hydrogen can vary, but is generally in the range of 1.23 to 1.48 volts, depending on the specific operating conditions and the electrodes used [3]. On the other hand, the potential required for the degradation of contaminants in sacrificial electrode electrochemical processes depends on the nature and concentration of the contaminants, as well as the efficiency of the process used [4].

Electrocatalytic hydrogen evolution has emerged as a popular method for hydrogen generation [5]. However, there are several issues, including cost-effectiveness, associated with these techniques. To address the dual challenges of the energy crisis and environmental pollution, sustainable photocatalytic hydrogen production has shown promise [6,7]. However, efficient photocatalytic hydrogen generation typically requires the use of external sacrificial agents or donors, such as alcohols or organic acids, to scavenge holes and reduce recombination [8]. The addition of these sacrificial agents increases the cost of hydrogen evolution, making it economically viable but less practical in the long run [9]. Thus, for a sustainable and efficient hydrogen evolution, there are two main requirements to achieve. Firstly, the photocatalyst must possess efficient electron-hole separation, numerous active reaction sites, and high visible light activity [10,11], which is crucial for effective hydrogen generation. The second challenge involves the recovery or generation of hydrogen energy from wastewater, enabling environmentally friendly and sustainable energy production combined with water treatment on a larger scale. This integrated approach holds promise for addressing both energy and environmental concerns.

Contaminants of emerging concern (CECs) are increasingly being detected in water sources worldwide, posing significant challenges to water quality and human health. These CECs include a wide range of pollutants, such as pharmaceuticals, personal care products, pesticides, industrial chemicals, and microplastics, which can enter water bodies through various pathways [12,13]. The presence of CECs in water raises concerns for both ecological and human health. These contaminants can have adverse effects on aquatic ecosystems, including the disruption of endocrine systems, alteration of reproductive behaviors, and changes in the composition of microbial communities. In terms of human health, exposure to CECs through drinking water consumption or recreational activities in contaminated water bodies can pose risks, particularly for vulnerable populations such as children and pregnant women [14].

Paracetamol (PTM), also known as acetaminophen, is a widely used over-the-counter medication for pain relief and fever reduction. Like many pharmaceuticals, it can enter the environment through various pathways, including improper disposal, excretion, and wastewater treatment plant effluents. While it is generally considered safe for human use when taken at recommended doses, the presence of PTM in water bodies as a CEC is a topic of growing interest and research. The presence of acetaminophen in aquatic environments can have adverse effects on aquatic organisms. Even at low concentrations, it can disrupt the endocrine systems of fish and other aquatic organisms, affecting their reproductive capabilities [15].

Thus, utilizing PTM as a sacrificial agent in photocatalytic hydrogen evolution serves both the purposes of clean energy generation and wastewater treatment.

Photoelectrochemical oxidation (PECO) is indeed a promising technique for the removal of PTM from water. PECO involves the use of a photoactive electrode, typically a semiconductor material, which generates reactive oxygen species (ROS) upon exposure to light. These ROS, such as hydroxyl radicals, play a crucial role in the degradation of organic contaminants like PTM [16].

Since the discovery of TiO_2's ability for water-splitting and photocatalytically degradation of organic compounds, numerous semiconductors have been studied for environmental and energy applications. TiO_2 is the most extensively investigated due to its chemical stability, low cost, and good photocatalytic efficiency [17]. However, TiO_2 does have a limitation in its optical response. With a large band gap (Eg. ~3.2 eV), TiO_2 primarily responds to UV light, which accounts for only 5% of solar energy [18]. To address this issue, various modifications of TiO_2 have been extensively studied to enhance its wavelength range response, promote charge generation, and facilitate efficient charge separation to minimize recombination [19]. Techniques for TiO_2 modifications include metal loading,

 doi:10.20944/preprints202401.2169.v1

ion doping, semiconductor coupling, and dye sensitization. Depositing precious metals or rare earth metals onto semiconductors is a widely investigated approach to enhance the photocatalytic properties of TiO_2 [20]. This method offers two main advantages: the formation of a Schottky junction for efficient charge separation and the localized surface plasmon resonance (LSPR) effect, which promotes enhanced charge generation through the absorption of visible light.

Pd and Pd-In catalysts have been widely reported in the catalytic reduction and electrochemical reduction of inorganic ions present in water [21–23]. It has been demonstrated that the Pd-In combination can hydrogenate nitrate ions into nitrites in water [24,25]. On the other hand, Pd has attracted significant attention as it is one of the platinum group metals with high catalytic activity for the hydrogen evolution reaction (HER) [26]. It is important to note that most of the catalysts, either mono- or bimetallic, based on Pd for the electrocatalytic production of H_2 implies the use of high metal loadings [27] which considerably increases the cost of these technologies. This work evaluates the catalytic performance of PdIn-doped TiO_2 catalysts (Pd, 1 wt.%, In 0.25 wt.%) in the photoelectrochemical oxidation of PTM and the simultaneous HER. The reaction mechanism, both for PTM oxidation and hydrogen evolution reaction (HER), and the stability of the catalyst is discussed.

2. Experimental

2.1. Catalyst synthesis

The bimetallic catalyst supported on titania was prepared using the conventional wet impregnation method by co-impregnating Pd:In in a 1:0.25 wt.% ratio relative to the support (TiO_2), followed by calcination and reduction.

A solution of $PdCl_2$ (Sigma Aldrich, p.a.), and +$InCl_3$ (Sigma Aldrich, 99.9%) was utilized to achieve the desired bimetallic catalyst [28]. The process involved adding a specific mass of TiO_2 support (Degussa, P25, 48 m^2/g) to a container containing water, along with a volume of concentrated Pd and In solutions, in order to attain the desired weight percentages of the metals, namely 1.00% Pd and 0.25% In.

Once the mixture was homogeneous and the solvent was evaporated, the material was dried overnight at 80°C, and then calcined at 500°C for 4 hours. Finally, it was reduced using a 0.2 M solution of hydrazine hydrate and washed several times with deionized water. The material was left to dry overnight at 80°C and named PdIn/TiO_2.

2.2. Physicochemical characterization

X-ray diffraction (XRD), energy-dispersive X-ray spectroscopy (EDX, N_2 adsorption-desorption isotherms were employed for the physicochemical characterization of catalysts.

XRD powder spectra were generated utilizing the X'Pert PRO X-ray diffractometer (PANalytical) to ascertain the crystal structure. The measurements were conducted using CuKα radiation (λ = 1.5405 Å) and the X'pert high score plus diffraction software. The 2θ data were collected in the range of 20° to 100° with a scanning rate of 0.04° s^{-1}. The identification of crystalline phases was achieved by comparing the experimental diffraction patterns with those in the Joint Committee on Powder Diffraction Standards (JCPDS).

Morphological characterization of the synthesized catalysts was performed by SEM images recorded with a ZEISS EVO 15 scanning electron microscope (SEM) with 2 nm resolution and Oxford X-MAX 50 mm^2 energy dispersive X-ray microanalyzer (EDX).

N_2 adsorption-desorption isotherms of the carbon supports were measured at -196 °C using a Micromeritics ASAP 2020 equipment. The total surface area was calculated from BET (Brunauer, Emmett and Teller) equation and the total pore volume was determined using the single point method at P/P0 = 0.99. Pore size distribution (PSD) curves were obtained from the analysis of the desorption branch of the N_2 isotherm using the BJH (Barrett, Joyner, and Halenda) method.

 doi:10.20944/preprints202401.2169.v1

2.3. Photochemical Properties

The materials were initially characterized using diffuse reflectance to obtain the band-gap values of the catalysts and narrow down the spectrum of catalysts to be studied. The band-gap values of each material were obtained using the Kubelka-Munk method (K-M or F(R)), as shown in Equation 1.

$$F(R) = \frac{(1-R)^2}{2R} \quad (1)$$

Where R is reflectance and F(R) is proportional to the extinction coefficient (α). A modified K-M function can be obtained by multiplying the F(R) function by $h\nu$, using the corresponding coefficient (n) associated with an electronic transition (Equation 2).

$$(F(R) * h\nu)^n \quad (2)$$

Graphing Equation 2 as a function of energy in eV yields the value of the material's band gap. The band gap refers to the energy difference between the valence band (the highest energy level filled with electrons) and the conduction band (the lowest empty energy level) in a material. The size of the band gap determines a material's ability to absorb light and participate in photochemical reactions. Therefore, materials with smaller band gaps are usually more efficient at utilizing a wider range of light energy, requiring less energy to promote electrons to the conduction band.

2.4. Electrochemical characterization

A temperature of 20°C was chosen to assess the electrochemical performance of the catalysts in a three-electrode cell controlled by a GAMRY Reference 620 – 45080 Potentiostat/Galvanostat. The reference electrode used was a reversible hydrogen electrode (RHE), and all potentials mentioned below are presented relative to this electrode. The counter electrode (CE) consisted of a glassy carbon (GC) rod, while the working electrode (WE) was applied as ink onto a GC disk. Assays in a rotating disk electrode (RDE) AUTOLAB RDE-2 were carried out under the same conditions. Current density values were obtained from the geometrical area of the WE.

For the preparation of the inks to be deposited on the GC disk, 2 mg of the catalyst was placed in an Eppendorf tube. Subsequently, 15 µL of NAFION and 500 µL of isopropyl alcohol were introduced into the tube, and the blend was subjected to 30 minutes of sonication for homogenization. After achieving homogeneity, the dispersed ink (40 µL) was applied onto a polished GC disk (10 mm diameter). The ink was then dried under an inert atmosphere before being utilized in the electrochemical cell. For assays in the RDE, 12 µL of the dispersed ink was applied onto the polished GC disk (3 mm diameter).

The electrochemical behavior of the catalyst powders in a phosphate buffer solution with and without PTM (100 mg.L^{-1}), purged with pure N_2 before each measurement, was examined using cyclic voltammetry (CV) and chronoamperometry techniques.

Electrolytic solutions were prepared using potassium phosphates salts (H_2KPO_4 and HK_2PO_4) and milli-Q water, to conform a solution 0.1 mol.L^{-1}, pH = 7.

Electroactive surface area was estimated from CV curves of the catalyst at different scan rates in the electrolyte support. CVs were performed for each material, including the bare electrode (i.e. glassy carbon), at different scan rates (5, 10, 20, 50, and 100 mV.s^{-1}) in the double-layer region to obtain the electroactive surface area (ECSA). The calculation of ECSA (equation 3) from the CV data involves the use of the electrochemical double-layer capacitance (EDLC), which can be obtained from the slope of the current density versus scan rate.

$$ECSA = R_f * S \quad (3)$$

Assuming that S is the geometric area of 0.785 cm^2, and R_f is the roughness factor obtained through equation 4.

 doi:10.20944/preprints202401.2169.v1

$$R_f = {}^{C_{dl}}/_{40\ \mu F * cm^{-2}} \quad (4)$$

Hydrodynamic voltammetry employing Rotating Disk Electrode (RDE) techniques was conducted. The rotation rate of the disk ranged from 750 rpm to 1750 rpm

2.5. Photoelectrochemical characterization

A Light source Xe lamp, XSS-5XD, (Power 150 to 320W, Radiant Output: 50W) was used to assessed the photoelectrochemical characterization of the materials. A light intensity of 57500 lux (lumen/m^2) were used for experiments.

Photoelectrochemical properties were evaluated by chronoamperometry and CV techniques in the presence and the absence of irradiation. The tests were carried out in a system as shown in the design in Figure 1. Temperature of the working solution was monitored along the experiments and no variations were discerned.

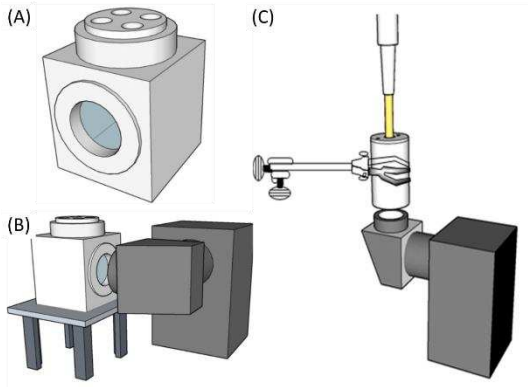

Figure 1. Illustration of the system (not to scale) used for photoelectrochemical assays. (A) Photoelectrochemical cell with four holes for RE, WE, AE, and recirculation of inert gas. (B) Arrangement of cell and lamp spaced 2 cm apart. (C) Arrangement for the RDE system.

3. Results and discussion

3.1. Characterization

UV-DRS analysis

To evaluate the absorbance properties of TiO_2 and PdIn/TiO_2 synthesized in this study, UV-Vis diffuse reflectance spectra (DRS) were measured (Figure 2). The absorption band edge of TiO_2 occurs at approximately 400 nm. The addition of PdIn leads to an increase in absorption at longer wavelengths within the visible range. The band gap values of TiO_2 and PdIn/TiO_2 were 3.67 and 3.47 eV, respectively. The lowest band gap value obtained after the impregnation of PdIn onto TiO_2 would indicate that the Pd, and In deposition enhances the light absorption capability, resulting in a possible higher catalytic activity when compared to TiO_2 alone. This behavior could be related to the Fermi levels of Pd, which is lower than that of TiO_2, facilitating the efficient transfer of photogenerated electrons from the conduction band of TiO_2 to the metal particles. This process of electron trapping greatly diminishes the rate of electron-hole recombination, leading to enhanced photocatalytic reactions.

 doi:10.20944/preprints202401.2169.v1

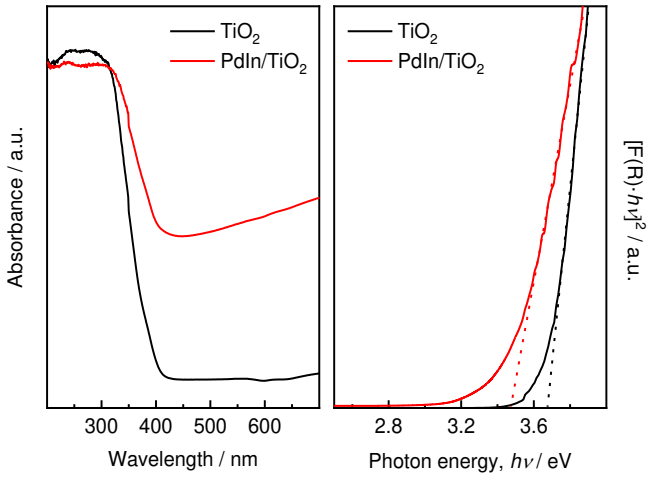

Figure 2. UV-vis absorption spectra (left panel) and bandgap energy plot (Kubelka–Munk function) of TiO_2 (black line) and $PdIn/TiO_2$ (red line) materials.

Physicochemical properties

Morphology and elemental analysis of $PdIn/TiO_2$ were studied by SEM, and SEM-EDS techniques, respectively. Figure 3 shows a SEM micrograph of $PdIn/TiO_2$ catalyst. A homogeneous distribution of the material was obtained, with a particle size of about 200 nm and dispersed agglomerates of 0.5 to 1 µm. By mapping and EDS analysis a high distribution of Pd and In on the TiO_2 particles was perceived, with average compositions of 0.89 ± 0.07 and 0.26 ± 0.07, respectively obtained from different regions of the catalyst. A Pd:In ratio (3.5) similar to the nominal value was observed.

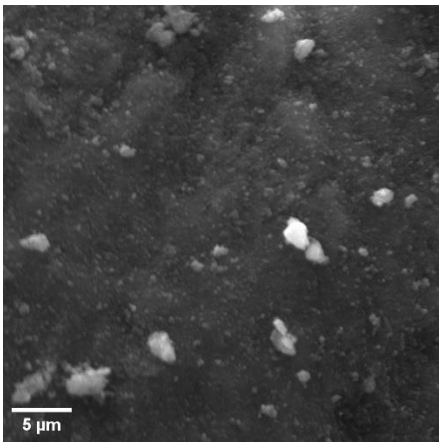

Figure 3. SEM micrograph of $PdIn/TiO_2$ material.

$PdIn/TiO_2$ surface area and pore volume, obtained from BET analysis, were 48.84 m^2/g and 0.0015 cm^3/g, respectively. For commercial TiO_2, a surface area of 50 m^2/g was reported [29]. Therefore, no diminution of the surface area is perceived after the metal deposition onto TiO_2 material.

XRD patterns of $PdIn/TiO_2$ and the bare support were assayed to elucidate the crystalline phases present. Figure 4 shows the corresponding diffractograms, respectively. Anatase (JCPDS 00-021-1272) and rutile (JCPDS 00-021-1276) phases were detected in both TiO_2 and $PdIn/TiO_2$ catalysts. No crystalline phases corresponding to Pd or In were detected, which could be due to the low metallic charge, the high dispersion of the material on the support and/or amorphous nature of the dispersed species. The crystallite size of both phases, anatase (plane 1 0 1, $2\theta = 25.281°$) and rutile (plane 1 1 0,

 doi:10.20944/preprints202401.2169.v1

2θ = 27.477°), for PdIn/TiO_2 and TiO_2 were calculated using Scherrer equation. Crystallite sizes of 20.93 nm were obtained for the anatase phase of both catalysts. For the rutile phase of TiO_2 and PdIn/TiO_2, crystallite sizes of 25.6 and 31.4 nm, respectively, were obtained. This change of crystallite size in the rutile phase could be due to a strong interaction with the metals Pd and In, or their introduction into its crystalline network, since the doping of the material could affect its electronic and structural properties and consequently the crystallite size [30–32].

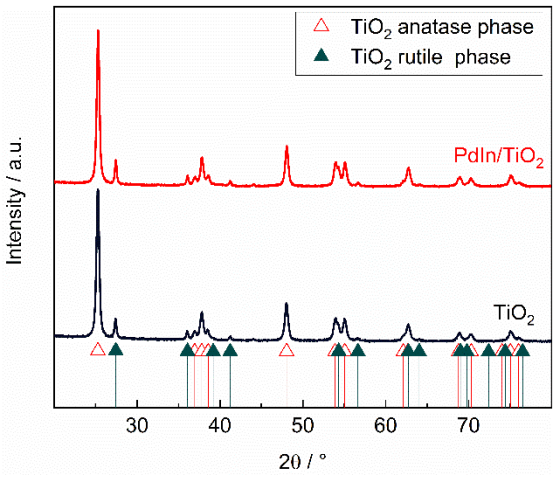

Figure 4. XRD patterns of PdIn/TiO_2 (red line) and TiO_2 (black line) samples.

The electroactive surface area was calculated by performing CVs at different scan rates in a potential range where no faradaic reaction occurs (i.e. capacitive current are employed), by plotting the anodic and cathodic current densities at a fixed potential versus the scanning rate (see Figure S1A in the supplementary material). Figure S1. B shows the current density as a function of scan rate ($mV.s^{-1}$) for GC. The same procedure was performed for TiO_2 and PdIn/TiO_2. The corresponding values of the EDLC and electroactive surface areas for the different electrodes, calculated using equations 3 and 4, are summarized in Table 1. Considering the slopes obtained for each material, it can be observed that PdIn/TiO_2 catalyst reveals higher ESA than GC and TiO_2.

Table 1. Double layer capacitance and electroactive surface area for the photoelectrocatalysts prepared.

Photocatalyst	$EDLC_A$ (mF/cm^2)	$EDLC_C$ (mF/cm^2)	Electroactive surface area (cm^2)
GC	0.00003	-0.00003	0.6
TiO_2	0.00011	-0.0001	2.5
PdIn/TiO_2	0.0004	-0.0004	8.24

3.2. Hydrogen evolution reaction (HER)

Figure 5 shows cyclic voltammograms performed at GC (black line), TiO_2 (red line) and PdIn/TiO_2 (blue line) between -0.3 V and 1.5 V in the electrolyte solution. As expected, GC electrode reveals only capacitive currents in the potential range under study. On the other hand, TiO_2 and PdIn/TiO_2 catalysts shows an increment of the cathodic current at potentials more negative than 0.0 V, which is associated to the HER. Interestingly, the presence of PdIn significantly improves the HER in the electrolyte solution. Indeed, PdIn/TiO_2 develops the double of current at -0.5 V in comparison with TiO_2. Remarkably, the catalytic activity toward the HER seems to be unaltered in the presence of paracetamol into the electrolyte solution (see Figure 8).

 doi:10.20944/preprints202401.2169.v1

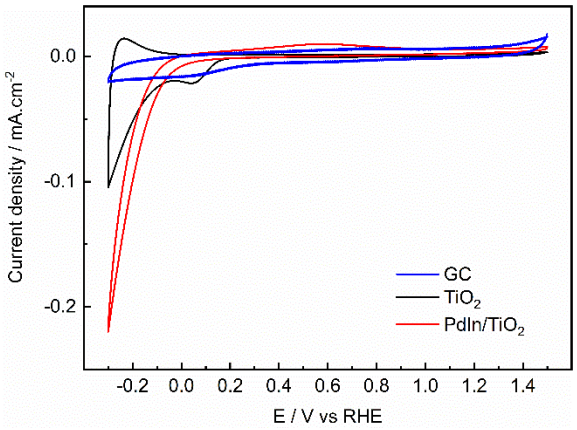

Figure 5. Cyclic voltammograms of GC (blue line), TiO_2 (black line) and $PdIn/TiO_2$ (red line) Sweep rate = 20 mV s^{-1}, in 0.1 M phosphate buffer solution, pH = 7, sweep rate = 20 mV s^{-1}.

The photoelectrocatalytic performance of TiO_2 (black lines) and $PdIn/TiO_2$ (red lines) catalysts toward the HER was evaluated through chronoamperometry technique in the presence (light on) and absence (light of) of radiation at 0 and -0.1 V with an irradiation intermittence of 30 seconds (Figure 6).

TiO_2 material develops low cathodic current and photocurrents at both studied potentials. Oppositely, $PdIn/TiO_2$ catalyst reveals high cathodic current values at both applied potentials and suitable photoactivity at 0.0 V. The decrease of the photoactivity of $PdIn/TiO_2$ at -0.1 V suggests that the flat band potential is close. In addition, $PdIn/TiO_2$ catalyst develops similar cathodic current values along the time, which indicate an appropriate photoelectrochemical stability and thus a suitable photoelectrocatalytic performance toward the HER.

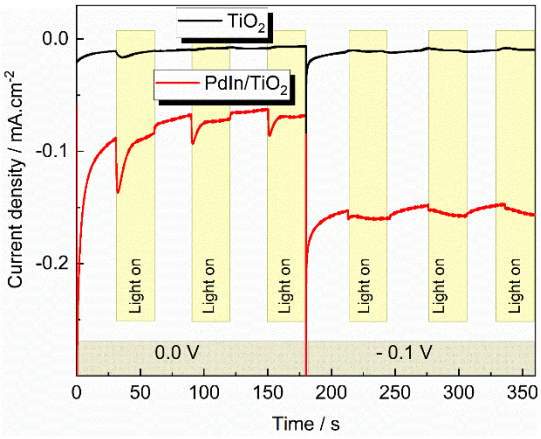

Figure 6. Current transients of TiO_2 (black line) and $PdIn/TiO_2$ (red line) recorded at 0.0 and -0.1 V in 0.1 M phosphate buffer solution, pH = 7, under the absence and the presence of light.

Tafel plot was employed to better understand the reaction kinetics and mechanism of the HER at the best catalyst developed in the current work. For this purpose, linear sweep voltammetry (LSV) was performed between 0.2 and -0.2 V at a sweep speed of 5 $mV.s^{-1}$. Two reaction mechanisms are commonly discussed in the literature [34,35], denoted as Volmer-Heyrovsky and Volmer-Tafel. Both mechanisms have in common that hydrogen is adsorbed (H_{ad}) on the electrode through the electrochemical Volmer step, but differ in the second stage, since for the Volmer-Heyrovsky (equation 5) mechanism, the Heyrovsky step (equation 6), the adsorbed hydrogen recombines with another proton from the solution to release a H_2 molecule. On the other hand, the Volmer-Tafel mechanism consists of two consecutive Volmer steps and the Tafel step (equation 7) in a recombination step of two adjacent hydrogen adsorbates to form H_2.

 doi:10.20944/preprints202401.2169.v1

$$Volmer: H_2O + e^- \rightleftharpoons H_{ad} + OH^- \quad (5)$$

$$Heyrovsky: H_{ad} + H_2O + e^- \rightleftharpoons H_2 + OH^- \quad (6)$$

$$Tafel: H_{ad} + H_{ad} \rightleftharpoons H_2 \quad (7)$$

Tafel slope values (TS) were employed to discern which reaction mechanism follows the HER at PdIn/TiO_2 catalyst. TS of 120, 30, and 40 mV dec^{-1} are associated with Volmer, Tafel, and Heyrovsky as rate determining step (RDS), respectively. Top panel of Figure 7 shows the LSV recorded for PdIn/TiO_2 performed at 5 $mv.s^{-1}$ from 0.2 V to -0.2 V in the electrolyte solution. Bottom panel of Figure 7 shows a TS close to 120 mV·dec^{-1} that is attributed to the Volmer step as the RDS during the HER at PdIn/TiO_2 catalyst. In this sense, the high TS may be attributed to the high amount of surface oxygenated species of TiO_2, which may inhibit the first electron transfer step.

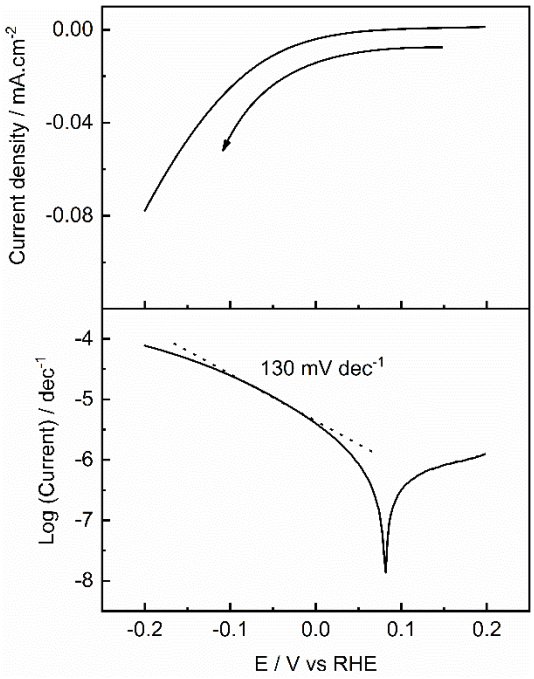

Figure 7. Linear sweep voltammogram recorded at 5 mV s^{-1} (top panel) and Tafel plot (bottom panel) for PdIn/TiO_2 in 0.1 M phosphate buffer solution, pH = 7.

3.3. Paracetamol oxidation reaction

The (photo)electrocatalytic activity of GCE, PdIn/TiO_2, and TiO_2 support towards the oxidation of PTM (100 ppm) was evaluated by cyclic voltammetry under irradiation and in the absence of irradiation. Figure 8 shows CVs profiles of PTM electrooxidation in the dark at GCE, TiO_2, and PdIn/TiO_2. As was discussed above (see Figure 5), the presence of PTM does not change the catalytic performance toward the HER at PdIn/TiO_2, and consequently the catalytic active sites for the HER are not compromised.

PTM oxidation on GCE (blue line) exhibits an anodic current generation with an anodic peak at 1.1V and an onset potential of 1.0 V. A quasi-reversible process with a peak-to-peak separation of ΔV = 250 mV was determined, as reported Nematollahi et al. [36] for the same material and similar pH conditions. At more positive potentials than the anodic current peak, a large drop in current density is observed, showing a Cottrell behavior, indicating that the process is limited by diffusion of the species towards the electrode surface.

On the other hand, TiO_2 (black line) and PdIn/TiO_2 (red line) show an irreversible behavior toward the PTM oxidation with onset potentials of 1.0 V and ΔV = 750 and 420 mV, respectively. Evidently, at higher potentials than the anodic peak current, the oxidation behavior is different for

 doi:10.20944/preprints202401.2169.v1

GCE in comparison with TiO_2-based materials. The last suggests that the reaction mechanism at TiO_2-based materials is limited by adsorbed species.

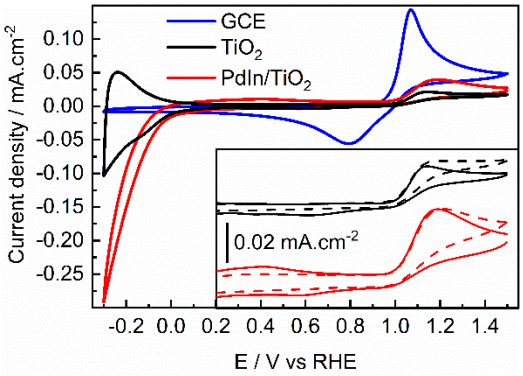

Figure 8. Cyclic voltammograms of GC (blue line), TiO_2 (black line) and PdIn/TiO_2 (red line) in a 100 ppm PTM solution in 0.1 M phosphate buffer solution. Sweep rate = 20 mV s^{-1}, pH = 7. Inset: TiO_2 and PdIn/TiO_2 in the absence (solid lines) and the presence of light (dashed lines) in a 100 ppm PTM solution in 0.1 M phosphate buffer solution. Sweep rate = 20 mV s^{-1}, pH = 7.

The same CV experiments were performed at TiO_2 and PdIn/TiO_2 but in the presence of light. The inset plot in Figure 8 compares voltammograms corresponding to the PTM oxidation at TiO_2 and PdIn/TiO_2 catalysts under the absence (solid lines) and the presence (dashed lines) of light. During the oxidation of PTM in the absence of light, at more positive potentials than the anodic peak, the current density slightly decreases (i.e. non-Cottrell behavior) with the rise of the applied potential suggesting that the current is limited by kinetic. Conversely, in the presence of light, the current density remained almost constant at more positive potentials than the anodic peak, which implies that the current is limited by kinetics and suggest adsorbed species as the responsible. On the other hand, during the reverse scan, the presence of light made the system completely irreversible, i.e. no cathodic currents are discerned.

To better understand the kinetics and reaction mechanism of the PTM oxidation at all materials studied in the current work, rotating disk experiments at different rotational speeds were performed.

Figure 9 compares CVs profiles of PTM oxidation at GCE performed at different sweep rates (top panel) and rotational rates (bottom panel). These experiments demonstrate that the PTM oxidation process is diffusion limited on the GCE, since, as shown in the bottom panel of figure 9, the anodic current density reaches a constant diffusion value (I_{DIF}), which increases with the growth of the rotational speed.

 doi:10.20944/preprints202401.2169.v1

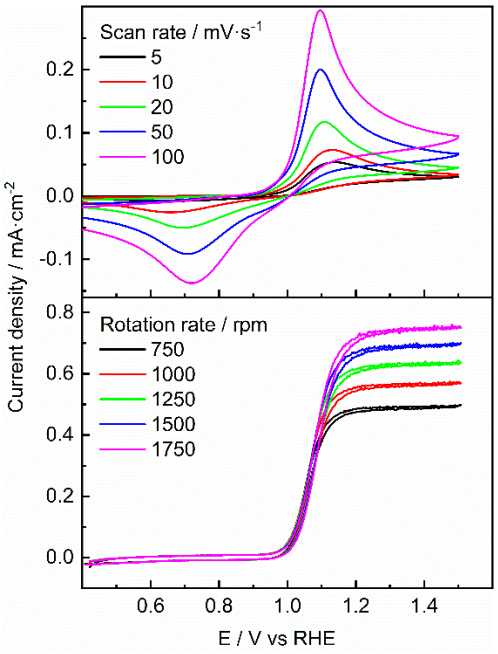

Figure 9. Cyclic voltammograms at diverse sweep rates (top panel) and steady-state polarization curves recorded at 10 mV s^{-1} at several rotation rates (bottom panel) at GCE in a 100 ppm PTM solution in 0.1 M phosphate buffer, pH = 7.

For GCE, Randles-Sevsick and Koutecky-Levich plot with the corresponding slope value is shown in Figure S2 (top panel) and S2 (bottom panel), respectively (obtained from Figure 9). Koutecky-Levich equation is shown in equation 8, where I_{DIF} is the limit current (A), I_k the kinetic current and I_{lev} is expressed by equation 9.

$$\frac{1}{I_{DIF}} = \frac{1}{I_{lev}} + \frac{1}{I_k} \tag{8}$$

$$I_{lev} = 0.62nFAD^{2/3}\omega^{1/2}\nu^{-1/6}C \tag{9}$$

v is the kinematic viscosity, w is the angular frequency of rotation (rad s^{-1}), A is the disk electrode area (cm^2), and other symbols have their conventional meanings. By plotting $\frac{1}{I_{DIF}}$ vs $\omega^{-1/2}$, and obtaining from literature the kinematic viscosity of the electrolyte (0.012 $cm^2 s^{-1}$) [37] and the diffusion coefficient D ($6.1x10^{-6}$ $cm^2.s^{-1}$) [38], the electron transferred number involved in the reaction yielded a value of 2, as Nematollahi et al. reported [36]. Thus, this process could be associated with the reversible transformation of PTM into N -acetyl- p -benzoquinone amine (NAPQI) [36]:

$$C_8H_9NO_2 \rightleftharpoons C_8H_7NO_2 + 2H^+ + 2e^- \tag{10}$$

On the other hand, the anodic peak potential for TiO_2 and PdIn/TiO_2 was plotted as a function of scan rate and a linear trend was discerned, which suggests that the process is limited by the adsorption of species on the electrode surface. The number of electrons (n) transferred to the surface of the electrode was calculated through the Laviron equation for an irreversible process, where α is the electron-transfer coefficient (0.5) and n is the number of electrons involved in the redox process [39].

$$E_{pA} = \frac{RT}{(1-\alpha)nF}\log(v) \tag{11}$$

For both TiO_2-based electrodes, the number of transferred electrons was 1 and the subsequent reaction is the most plausible to occur:

$$C_8H_9NO_2 \rightleftharpoons (C_8H_8NO_2)_{ad} + H^+ + 1e^- \tag{12}$$

 doi:10.20944/preprints202401.2169.v1

Then, the adsorbed species may follow subsequent reactions at more positive potentials:

$$(C_8H_8NO_2)_{ad} \rightleftharpoons (C_8H_7NO_2)_{ad} + H^+ + 1e^- \quad (13)$$

$$(C_8H_7NO_2)_{ad} \rightleftharpoons C_8H_7NO_2 \quad (14)$$

$$(C_8H_7NO_2)_{ad} + 14H_2O \rightharpoonup 8CO_2 + \frac{1}{2}N_2 + 35H^+ + 35e^- \quad (15)$$

Equation (14) seems to be facile at GCE, while the opposite happens at TiO_2-based electrodes and accordingly the adsorbate path is favored. In this sense, equation (15) indicates the global reaction toward the total mineralization of paracetamol, which is expected to follows the adsorbate route by deprotonation processes. In this context, it is important to note that the presence of radiation at TiO_2-based electrodes completely inhibits the pathway toward soluble species (i.e. eq. 14), and consequently no cathodic peaks are detected during the reverse sweep.

In this regard, bottom panel of Figure 10 suggests the aforementioned due to a subsequent increment of the anodic current is perceived with the rise of applied potential in the presence of light. Remarkably, the same current values were obtained at higher rotation rates than 750 rpm and no inhibition was discerned with the subsequent cycles. Therefore, the adsorbate route seems to occur at TiO_2-based catalysts. Furthermore, small amount of PdIn into TiO_2 not only increase the catalytic efficiency toward the PTM oxidation, but also intensely raise the HER, which is no inhibited in the presence of the organic molecule.

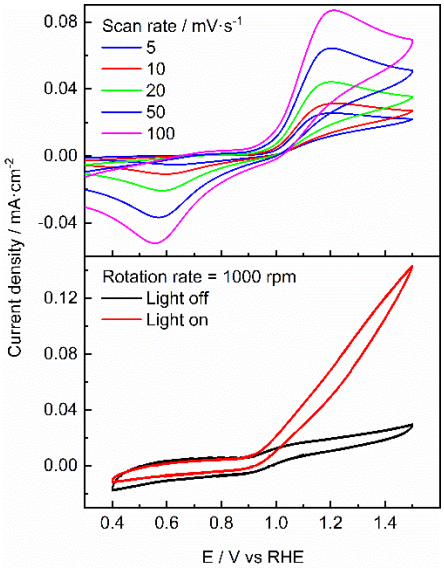

Figure 10. PTM oxidation at diverse sweep rates (top panel) and steady-state polarization curves for 100 ppm PTM oxidation recorded at 10 mV s^{-1} at 1000 rpm (bottom panel) at PdIn/TiO_2 electrode. 100 ppm of PTM in 0.1 M phosphate buffer solution, pH = 7.

Finally, in order to test the catalytic stability of PdIn/TiO_2 toward the degradation of PTM in absence and the presence of light, a current transient was recorded at 1.2 V and depicted in Figure 11. An initial decrease in the anodic current density in the absence of light is observed, which rises and remains almost constant when the system is exposed to light. The last indicates an improved catalyst performance toward the PTM photoelectroxidation.

 doi:10.20944/preprints202401.2169.v1

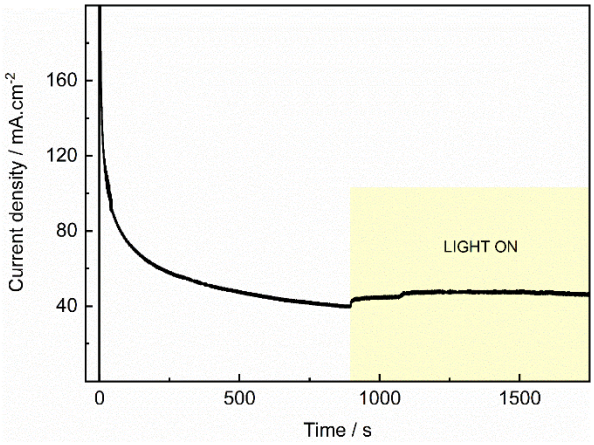

Figure 11. Photo/current transients of PdIn/TiO_2 recorded at 1.2 V at 1000 rpm, under the absence and the presence of light in a 100 ppm PTM solution in 0.1 M phosphate buffer solution, pH = 7.

4. Conclusions

The deposition of Pd and In enhanced the light absorption capacity, and led to a notable improvement for the hydrogen evolution reaction (HER), with the rate determining step of H_2 generation corresponding to the Volmer step, when compared to TiO_2. This improvement is observed not only in the electrolyte but also in the presence of paracetamol. In the context of PTM oxidation, both TiO_2 and PdIn/TiO_2 exhibit an irreversible behavior, primarily hindered by the adsorption of species on the electrode surface. The presence of radiation at TiO_2-based electrodes completely inhibits the pathway toward soluble species resulting in a completely irreversible process and improved the catalyst performance toward the PTM photoelectroxidation.

Thus, a small amount of PdIn into TiO_2 not only increase the catalytic efficiency toward the PTM oxidation, but also intensely raise the HER, which is no inhibited in the presence of the organic molecule, highlighting its capability for both environmental remediation and the sustainable production of hydrogen.

Consequently, PdIn-doped TiO_2 emerges as a promising catalyst, showcasing heightened physicochemical properties and superior catalytic performance. This highlights its potential for applications in both environmental remediation and sustainable hydrogen production.

Supplementary Materials: The following supporting information can be downloaded at the website of this paper posted on Preprints.org.

CRediT authorship contribution statement: Conceptualization, **G.G.**, **N.S.**, **F.A.M**, and **I.G.**; Methodology, **N.S.** and **A.I.** and **I.G.**; Formal analysis, **G.G.**, **N.S.** and **F.A.M.**; data curation, **N.S.**, and **A.I.**; writing-review and editing, **G.G.**, and **N.S.**, funding acquisition, **G.G.** and **F.A.M.** All authors have read and agreed to the published version of the manuscript.

Funding: Ministry of Science, Technology, and Innovation (MinCyT).

Informed Consent Statement: Not applicable.

Acknowledgments: The authors would like to thank the Ministry of Science, Technology, and Innovation (MinCyT) for the funding provided for the funding granted for "Academic and Professional Training Internships abroad for Argentines". In addition, this work has been supported by the Ministerio de Ciencia e Innovación (MCIN) under projects PCI2020-112249 and PID2020-117586RB-I00 funded by MCIN/AEI/10.13039/501100011033, and by the Agencia Canaria de Investigación, Innovación y Sociedad de la Información (ACIISI, ProID2021010098). G.G. thanks NANOtec, INTech, the Cabildo de Tenerife and ULL.

Conflicts of Interest: The authors declare no conflict of interest.

References

1. Feng, C.; Chen, Z.; Jing, J.; Sun, M.; Tian, J.; Lu, G.; Ma, L.; Li, X.; Hou, J. Significantly Enhanced Photocatalytic Hydrogen Production Performance of G-C_3N_4/CNTs/CdZnS with Carbon Nanotubes as the Electron Mediators. *J Mater Sci Technol* **2021**, *80*, 75–83, doi:10.1016/j.jmst.2020.11.047.
2. Kim, D.; Yong, K. Boron Doping Induced Charge Transfer Switching of a C_3N_4/ZnO Photocatalyst from Z-Scheme to Type II to Enhance Photocatalytic Hydrogen Production. *Appl Catal B* **2021**, *282*, doi:10.1016/j.apcatb.2020.119538.
3. Fernandez-Ibanez, P.; McMichael, S.; Rioja Cabanillas, A.; Alkharabsheh, S.; Tolosana Moranchel, A.; Byrne, J.A. New Trends on Photoelectrocatalysis (PEC): Nanomaterials, Wastewater Treatment and Hydrogen Generation. *Curr Opin Chem Eng* **2021**, *34*, 100725, doi:10.1016/j.coche.2021.100725.
4. Truong, H.B.; Bae, S.; Cho, J.; Hur, J. Advances in Application of g–C_3N_4–Based Materials for Treatment of Polluted Water and Wastewater via Activation of Oxidants and Photoelectrocatalysis: A Comprehensive Review. *Chemosphere* **2022**, *286*, 131737, doi:10.1016/j.chemosphere.2021.131737.
5. Xie, L.; Wang, L.; Zhao, W.; Liu, S.; Huang, W.; Zhao, Q. WS_2 Moiré Superlattices Derived from Mechanical Flexibility for Hydrogen Evolution Reaction. *Nat Commun* **2021**, *12*, doi:10.1038/s41467-021-25381-1.
6. Yang, Z. zhu; Zhang, C.; Zeng, G. ming; Tan, X. fei; Huang, D. lian; Zhou, J. wu; Fang, Q. zhen; Yang, K. hua; Wang, H.; Wei, J.; et al. State-of-the-Art Progress in the Rational Design of Layered Double Hydroxide Based Photocatalysts for Photocatalytic and Photoelectrochemical H_2/O_2 Production. *Coord Chem Rev* 2021, *446*.
7. Wang, L.; Xie, L.; Zhao, W.; Liu, S.; Zhao, Q. Oxygen-Facilitated Dynamic Active-Site Generation on Strained MoS_2 during Photo-Catalytic Hydrogen Evolution. *Chemical Engineering Journal* **2021**, *405*, doi:10.1016/j.cej.2020.127028.
8. Chen, Z.; Li, S.; Peng, Y.; Hu, C. Tailoring Aromatic Ring-Terminated Edges of g-C_3N_4nanosheets for Efficient Photocatalytic Hydrogen Evolution with Simultaneous Antibiotic Removal. *Catal Sci Technol* **2020**, *10*, 5470–5479, doi:10.1039/d0cy00898b.
9. Kumar, A.; Sharma, G.; Kumari, A.; Guo, C.; Naushad, M.; Vo, D.V.N.; Iqbal, J.; Stadler, F.J. Construction of Dual Z-Scheme g-C3N4/$Bi_4Ti_3O_{12}$/$Bi_4O_5I_2$ Heterojunction for Visible and Solar Powered Coupled Photocatalytic Antibiotic Degradation and Hydrogen Production: Boosting via I^-/I^{3-} and Bi^{3+}/Bi^{5+} Redox Mediators. *Appl Catal B* **2021**, *284*, doi:10.1016/j.apcatb.2020.119808.
10. Sharma, G.; Dionysiou, D.D.; Sharma, S.; Kumar, A.; Al-Muhtaseb, A.H.; Naushad, M.; Stadler, F.J. Highly Efficient Sr/Ce/Activated Carbon Bimetallic Nanocomposite for Photoinduced Degradation of Rhodamine B. *Catal Today* **2019**, *335*, 437–451, doi:10.1016/j.cattod.2019.03.063.
11. Zhang, S.; Wang, L.; Liu, C.; Luo, J.; Crittenden, J.; Liu, X.; Cai, T.; Yuan, J.; Pei, Y.; Liu, Y. Photocatalytic Wastewater Purification with Simultaneous Hydrogen Production Using MoS_2 QD-Decorated Hierarchical Assembly of $ZnIn_2S_4$ on Reduced Graphene Oxide Photocatalyst. *Water Res* **2017**, *121*, 11–19, doi:10.1016/j.watres.2017.05.013.
12. Priyadarshini, M.; Sathe, S.M.; Ghangrekar, M.M. Hybrid Treatment Solutions for Removal of Micropollutant From Wastewaters. In *Microconstituents in the Environment*; Wiley, 2023; pp. 491–512.
13. Babuji, P.; Thirumalaisamy, S.; Duraisamy, K.; Periyasamy, G. Human Health Risks Due to Exposure to Water Pollution: A Review. *Water (Basel)* **2023**, *15*, 2532, doi:10.3390/w15142532.
14. Inostroza, P.A.; Carmona, E.; Arrhenius, Å.; Krauss, M.; Brack, W.; Backhaus, T. Target Screening of Chemicals of Emerging Concern (CECs) in Surface Waters of the Swedish West Coast. *Data (Basel)* **2023**, *8*, 93, doi:10.3390/data8060093.
15. Ameliorative Effects of Frankincense Oil on Rats Treated with a Minimum Toxic Dose of Paracetamol. *Journal of Medical and Life Science* **2023**, *0*, 0–0, doi:10.21608/jmals.2023.308224.
16. Sacco, N.A.; Marchesini, F.A.; Gamba, I.; García, G. Photoelectrochemical Degradation of Contaminants of Emerging Concern with Special Attention on the Removal of Acetaminophen in Water-Based Solutions. **2023**, 1–22.
17. Hashimoto, K.; Irie, H.; Fujishima, A. TiO_2 Photocatalysis: A Historical Overview and Future Prospects. *Japanese Journal of Applied Physics, Part 1: Regular Papers and Short Notes and Review Papers* **2005**, *44*, 8269–8285, doi:10.1143/JJAP.44.8269.
18. Daghrir, R.; Drogui, P.; Robert, D. Modified TiO2 for Environmental Photocatalytic Applications: A Review. *Ind Eng Chem Res* 2013, *52*, 3581–3599.
19. Ni, M.; Leung, M.K.H.; Leung, D.Y.C.; Sumathy, K. A Review and Recent Developments in Photocatalytic Water-Splitting Using TiO_2 for Hydrogen Production. *Renewable and Sustainable Energy Reviews* 2007, *11*, 401–425.
20. Yilmaz, P.; Lacerda, A.M.; Larrosa, I.; Dunn, S. Photoelectrocatalysis of Rhodamine B and Solar Hydrogen Production by TiO_2 and Pd/TiO_2 Catalyst Systems. *Electrochim Acta* **2017**, *231*, 641–649, doi:10.1016/j.electacta.2017.02.035.

21. Marchesini, F.A.; Mendow, G.; Picard, N.P.; Zoppas, F.M.; Aghemo, V.S.; Gutierrez, L.B.; Querini, C.A.; Miró, E.E. PdIn Catalysts in a Continuous Fixed Bed Reactor for the Nitrate Removal from Groundwater. *International Journal of Chemical Reactor Engineering* **2019**, *17*, 1–17, doi:10.1515/ijcre-2018-0126.
22. Beltrame, T.F.; Zoppas, F.M.; Ferreira, J.Z.; Marchesini, F.A.; Bernardes, A.M. Nitrate Reduction by Electrochemical Processes Using Copper Electrode: Evaluating Operational Parameters Aiming Low Nitrite Formation. *Water Science and Technology* **2021**, *84*, 200–215, doi:10.2166/wst.2021.215.
23. Beltrame, T.F.; Zoppas, F.M.; Gomes, M.C.; Ferreira, J.Z.; Marchesini, F.A.; Bernardes, A.M. Electrochemical Nitrate Reduction of Brines: Improving Selectivity to N_2 by the Use of Pd/Activated Carbon Fiber Catalyst. *Chemosphere* **2021**, *279*, 130832, doi:10.1016/j.chemosphere.2021.130832.
24. Marchesini, F.A.; Irusta, S.; Querini, C.; Miró, E. Spectroscopic and Catalytic Characterization of Pd-In and Pt-In Supported on Al_2O_3 and SiO_2, Active Catalysts for Nitrate Hydrogenation. *Appl Catal A Gen* **2008**, *348*, 60–70, doi:10.1016/j.apcata.2008.06.026.
25. Marchesini, F.A.; Gutierrez, L.B.; Querini, C.A.; Miró, E.E. Pt,In and Pd,In Catalysts for the Hydrogenation of Nitrates and Nitrites in Water. FTIR Characterization and Reaction Studies. *Chemical Engineering Journal* **2010**, *159*, 203–211, doi:10.1016/j.cej.2010.02.056.
26. Sarkar, S.; Peter, S.C. An Overview on Pd-Based Electrocatalysts for the Hydrogen Evolution Reaction. *Inorg Chem Front* 2018, *5*, 2060–2080.
27. Sarkar, S.; Peter, S.C. An Overview on Pd-Based Electrocatalysts for the Hydrogen Evolution Reaction. *Inorg Chem Front* 2018, *5*, 2060–2080.
28. Sacco, N.A.; Zoppas, F.M.; Aghemo, V.S.; Beltrame, T.F.; Marchesini, F.A. Pd / In-Based Catalysts for Nitrate Catalytic Removal from Water: Synthesis Designs Aiming for Better N_2 Selectivity. *Water Supply* **2023**, *00*, 1–20, doi:10.2166/ws.2023.019.
29. Merino-Garcia, I.; García, G.; Hernández, I.; Albo, J. An Optofluidic Planar Microreactor with Photoactive $Cu_2O/Mo_2C/TiO_2$ heterostructures for Enhanced Visible Light-Driven CO2conversion to Methanol. *Journal of CO_2 Utilization* **2023**, *67*, doi:10.1016/j.jcou.2022.102340.
30. Yang, Y.-K.; Jiao, C.-Q.; Meng, Y.-S.; Yao, N.-T.; Jiang, W.-J.; Liu, T. Substituent Effect on Metal-to-Metal Charge Transfer Behavior of Cyanide-Bridged $\{Fe_2Co_2\}$ Square. *Inorg Chem Commun* **2021**, *130*, 108712, doi:10.1016/j.inoche.2021.108712.
31. Chavez Zavaleta, R.; Fomichev, S.; Khaliullin, G.; Berciu, M. Effects of Reduced Dimensionality, Crystal Field, Electron-Lattice Coupling, and Strain on the Ground State of a Rare-Earth Nickelate Monolayer. *Phys Rev B* **2021**, *104*, 205111, doi:10.1103/PhysRevB.104.205111.
32. Dehury, T.; Kumar, S.; Rath, C. Structural Transformation and Bandgap Engineering by Doping Pr in HfO_2 Nanoparticles. *Mater Lett* **2021**, *302*, 130413, doi:10.1016/j.matlet.2021.130413.
33. Zhang, H.; Li, Y.; Zhang, G.; Xu, T.; Wan, P.; Sun, X. A Metallic CoS_2 Nanopyramid Array Grown on 3D Carbon Fiber Paper as an Excellent Electrocatalyst for Hydrogen Evolution. *J Mater Chem A Mater* **2015**, *3*, 6306–6310, doi:10.1039/c5ta00707k.
34. Bazan-Aguilar, A.; García, G.; Pastor, E.; Rodríguez, J.L.; Baena-Moncada, A.M. In-Situ Spectroelectrochemical Study of Highly Active Ni-Based Foam Electrocatalysts for Hydrogen Evolution Reaction. *Appl Catal B* **2023**, *336*, 122930, doi: 10.1016/j.apcatb.2023.122930.
35. López, M.; Exner, K.S.; Viñes, F.; Illas, F. Theoretical Study of the Mechanism of the Hydrogen Evolution Reaction on the V_2C MXene: Thermodynamic and Kinetic Aspects. *J Catal* **2023**, *421*, 252–263, doi: 10.1016/j.jcat.2023.03.027.
36. Nematollahi, D.; Shayani-Jam, H.; Alimoradi, M.; Niroomand, S. Electrochemical Oxidation of Acetaminophen in Aqueous Solutions: Kinetic Evaluation of Hydrolysis, Hydroxylation and Dimerization Processes. *Electrochim Acta* **2009**, *54*, 7407–7415, doi: 10.1016/j.electacta.2009.07.077.
37. Chenlo, F.; Moreira, R.; Pereira, G.; Vá zquez, M.J. *Viscosity of Binary and Ternary Aqueous Systems of NaH_2PO_4, Na_2HPO_4, Na_3PO_4, KH_2PO_4, K_2HPO_4, and K_3PO_4. The Kinematic Viscosities of Aqueous Solutions of NaH*; 1996;
38. Pournaghi-Azar, M.H.; Kheradmandi, S.; Saadatirad, A. Simultaneous Voltammetry of Paracetamol, Ascorbic Acid, and Codeine on a Palladium-Plated Aluminum Electrode: Oxidation Pathway and Kinetics. *Journal of Solid State Electrochemistry* **2010**, *14*, 1689–1695, doi:10.1007/s10008-010-1011-2.
39. Zoubir, J.; Bakas, I.; Assabbane, A. A Simple Platform for the Electro-Catalytic Detection of the Dimetridazole Using an Electrochemical Sensor Fabricated by Electro-Deposition of Ag on Carbon Graphite: Application: Orange Juice, Tomato Juice and Tap Water. *Heliyon* **2021**, *7*, doi:10.1016/j.heliyon.2021.e07542.